Journal of Computational Physics 508 (2024) 112981

Contents lists available at ScienceDirect

Journal of Computational Physics

journal homepage: www.elsevier.com/locate/jcp

A non-oscillatory finite volume scheme using a weighted smoothed reconstruction

Davoud Mirzaei [a,*], Navid Soodbakhsh [b,c]

[a] Division of Scientific Computing, Department of Information Technology, Uppsala University, Sweden
[b] Department of Applied Mathematics and Computer Science, Faculty of Mathematics and Statistics, University of Isfahan, 81746-73441, Isfahan, Iran
[c] School of Mathematics, Institute for Research in Fundamental Sciences (IPM), Tehran, 19395-5746, Iran

ARTICLE INFO

Keywords:
Conservation laws
Finite volume method
Radial basis functions
Polyharmonic splines
Weighted smoothed reconstruction (WSR)

ABSTRACT

In this research article, we introduce a high-order and non-oscillatory finite volume method in combination with radial basis function approximations and use it for the solution of scalar conservation laws on unstructured meshes. This novel approach departs from conventional non-oscillatory techniques, which often require the use of multiple stencils to achieve smooth reconstructions. Instead, the new method uses a single central stencil and hinges on an approximate interpolation methodology called the weighted smoothed reconstruction (WSR), with a foundation on polyharmonic spline interpolation. Through some numerical experiments, we demonstrate the efficiency and accuracy of the new approach. It reduces the computational cost and performs well in capturing shocks and sharp solution fronts.

1. Introduction

Many physics and engineering problems give rise to time-dependent partial differential equations (PDEs), and one of the most significant and extensively used among them is the hyperbolic conservation law. A characteristic feature of conservation laws is that the solution to the problem may develop discontinuities (shocks) or sharp fronts, even when the initial condition is smooth. These discontinuities or sharp fronts result in non-physical oscillations in the numerical solution. The purpose of numerical techniques is to precisely capture these discontinuities (shocks) while avoiding unphysical oscillations and achieving a solution with a high order of convergence.

Over recent decades, the finite volume method (FVM) has been established as a well-known and commonly used numerical technique for solving conservation laws. FVM holds a rich history, and has been evolved into various forms and methodologies [31,34,38,51]. The main structure behind almost all finite volume methods is the spatial discretization of the domain into a set of cells (control volumes), temporal discretization of time interval, reconstructing the solution in each control volume using the given cell average values (average of the solution in a control volume) at a certain time, and then updating the cell average values in the next time step by calculating the numerical flux at the cell interfaces. These methods are either *linear* or *non-linear* and share similarities with finite difference schemes for hyperbolic PDEs, but are also adaptable to unstructured grids.

According to the Godunov theorem a linear scheme must be either only first-order accurate or oscillatory. Some nonlinear numerical schemes have been developed towards high-order non-oscillatory methods, including artificial viscosity schemes, total variation

* Corresponding author.
E-mail address: davoud.mirzaei@it.uu.se (D. Mirzaei).

https://doi.org/10.1016/j.jcp.2024.112981
Received 6 October 2023; Received in revised form 29 February 2024; Accepted 28 March 2024

Available online 3 April 2024

diminishing (TVD) schemes, total variation bounded (TVB) schemes, essentially non-oscillatory (ENO) and weighted essentially non-oscillatory (WENO) schemes, monotonicity-preserving schemes, and boundary variation diminishing (BVD) schemes. There are typically three approaches employed in these techniques: *Godunov's approach*, the use of *artificial viscosity*, or the use of a *high-order reconstruction*. Standard numerical methods of Godunov-type are well introduced in LeVeque [34] and Toro [51], Hesthaven [17], and references therein in the context of FVM. A finite difference artificial viscosity method was proposed by Von Neumann and Richtmyer [52] in the 1950s. Then it becomes the predominant approach in the finite element method (FEM) community for solving fluid dynamic problems [14,21,28,39]. As an application of the artificial viscosity and hyperviscosity methods for stabilizing RBF-based algorithms refer to [41,50].

The earliest attempts at achieving higher than first-order *reconstructions* date back to the application of flux and slope limiter methods to obtain second-order accurate schemes in FVM [34]. Subsequently, higher-order ENO reconstructions were developed and widely used for approximating hyperbolic PDEs in computational fluid dynamic problems [1,15,16,46–48]. The primary idea behind the ENO reconstruction includes determining sets of stencils surrounding a control volume, then computing a reconstruction on each of these stencils, and then picking the smoothest (least oscillatory) reconstruction as the desired reconstruction on the control volume. The ENO reconstruction on a control volume can be improved by using a weighted sum of different reconstructions on different stencils. The weights are chosen based on the smoothness of the reconstructions, such that smoother (least oscillatory) reconstructions have higher weights. This technique is known as WENO reconstruction (see for example [10,20,27,35,42,43,55,57]). A comprehensive review of this approach in FDM and FVM frameworks, using polynomial reconstructions, can be found in [44]. Efforts to combine WENO schemes with RBF interpolations were made earlier in [2,3,23].

Another class of reconstruction techniques are central essentially non-oscillatory (CENO) methods that aim to overcome some restriction of ENO/WENO methods by using a central reconstruction through combining a high-order k-exact and a monotonicity preserving piecewise linear reconstructions [24].

In this article, we introduce a novel non-oscillatory finite volume method that adeptly captures shocks and sharp fronts in the solution using just one central stencil. This places it within the CENO category, although it fundamentally differs from the existing CENO methods. Our approach employs a single central stencil alongside a generalized spline smoothing technique, called *weighted smoothed reconstruction* (WSR), to suppress non-physical oscillations in the vicinity of shocks or sharp fronts. This stands in contrast to the WENO reconstruction method, which involves the selection of several stencils (central, forward, and backward), computation of corresponding reconstructions, and forming a weighted reconstruction by assigning specific weights to different reconstructions.

To achieve a non-oscillatory reconstruction, we extend the approximate interpolation method presented in [54] to a weighted smoothed approximation with varying smoothing parameters. This WSR approach is based on radial basis function (RBF) approximation and is integrated into the reconstruction step of the finite volume method (FVM). When comparing it to other techniques, we denote this method as FVM-WSR. It is applicable to unstructured meshes and can be adapted for various kernel-based interpolations. To ensure stability and accuracy, we employ polyharmonic spline basis functions and use their scalability properties to construct stable local interpolation matrices. In the temporal domain, we use strong stability-preserving Runge-Kutta (SSPRK) methods [6,11,12,46].

The structure of this paper is as follows: In Section 2, we provide a brief overview of kernel-based interpolation and polyharmonic spline RBF approximation. In Section 3, we outline the fundamental principles of FVM for conservation laws and briefly discuss the WENO reconstruction. In Section 4, we explore the approximate interpolation and the smoothing spline technique, and then develop the generalized version WSR that will be employed in subsequent sections. In Section 5 we focus on the adaptation of the WSR technique for use in the FVM framework, and finally in Section 6, we demonstrate the performance and accuracy of FVM-WSR in solving various types of scalar conservation laws, including linear advection, Burgers', and the Kurganov-Petrova-Popov (KKP) equations, both with smooth and discontinuous initial conditions.

2. RBF interpolation

In this section, we provide a short overview of standard interpolation using conditionally positive definite kernels. For more details see, for example, [9,53].

Assume that $\mathbb{R}^d$ represents the set of all real vectors in dimension d, and $\|\cdot\|$ stands for the Euclidean norm on $\mathbb{R}^d$. Also, assume that $\mathbb{P}^d_m$ is the space of polynomials of degree at most m (order $m+1$) on $\mathbb{R}^d$. The dimension of this space is $Q = \binom{m+d}{d}$.

Definition 2.1. A univariate, continuous and even function ϕ is conditionally positive definite on $\mathbb{R}^d$ with respect to polynomial space $\mathbb{P}^d_m$ (or of order $m+1$) if

$$\sum_{i=1}^{N}\sum_{j=1}^{N}\alpha_i\alpha_j\phi(\|x_i - x_j\|) > 0$$

for any N and any set of pairwise distinct points $x_1, x_2, \dots, x_N \in \mathbb{R}^d$ and any real values $\alpha_1, \alpha_2, \dots, \alpha_N$ that satisfy the side condition

$$\sum_{j=1}^{N}\alpha_j p(x_j) = 0, \quad \text{for all } p \in \mathbb{P}^d_m.$$

Table 1
Typical RBFs for $r = \|x\|_2$, $x \in \mathbb{R}^d$.

RBF	$\phi(r)$	Parameters	Order
Gaussian	$\exp(\varepsilon^2 r^2)$	$\varepsilon > 0$	0
Sobolev spline	$r^{\beta-d/2} K_{\beta-d/2}(\varepsilon r)$	$\beta > d/2$, $\varepsilon > 0$	0
IMQ	$(1+\varepsilon^2 r^2)^{-\beta}$	$\beta > 0$, $\varepsilon > 0$	0
MQ	$(1+\varepsilon^2 r^2)^{\beta}$	$\beta > 0$, $\beta \notin \mathbb{N}$, $\varepsilon > 0$	$\lceil \beta \rceil$
Polyharmonic splines (PHS)	$\begin{cases} r^{2k-d}\log r \\ r^{2k-d} \end{cases}$	$k \in \mathbb{N}$, d even $k \in \mathbb{N}$, d odd	$k - \lceil d/2 \rceil + 1$
Wendland's functions	$\phi_{d,k}(\varepsilon r)$	$k \in \mathbb{N}_0$, $d \in \mathbb{N}$, $\varepsilon > 0$	0

Function ϕ is called positive definite if it is conditionally positive definite of order zero. Such a (conditionally) positive definite function is called a radial basis function (RBF).

Some typical examples of RBF $\phi(r)$ for $r = \|x\|_2$, $x \in \mathbb{R}^d$, are listed in Table 1. The positive parameter ε is called the shape parameter. Polyharmonic spline (PHS) kernels are examples of ε-free RBFs. In the second row of the table, K_β is the modified Bessel function of the second kind of order β. For explicit formula of Wendland's functions $\phi_{d,k}(\varepsilon r)$ see [53, Chapter 9].

The RBF interpolation of a continuous function $f : \Omega \subset \mathbb{R}^d \to \mathbb{R}$ on a discrete set $X = \{x_1, \dots, x_N\} \subset \Omega$ is expressed as follows

$$s_{f,X}(x) = \sum_{j=1}^{N} \alpha_j \phi(\|x - x_j\|) + \sum_{j=1}^{Q} \beta_j p_j(x) \tag{2.1}$$

where $\{p_1, \dots, p_Q\}$ forms a basis for $\mathbb{P}_m^d$. Imposing the interpolation conditions $s_{f,X}(x_i) = f(x_i)$ for $i = 1, \dots, N$, and applying the above side condition imply that the vectors $\alpha = (\alpha_1, \dots, \alpha_N)^T$ and $\beta = (\beta_1, \dots, \beta_Q)^T$ satisfy the system of equations

$$\begin{bmatrix} A & P \\ P^T & 0 \end{bmatrix} \begin{bmatrix} \alpha \\ \beta \end{bmatrix} = \begin{bmatrix} f_X \\ 0 \end{bmatrix} \tag{2.2}$$

where

$$\begin{aligned} A &= (\phi(\|x_j - x_i\|)) \in \mathbb{R}^{N\times N}, \\ P &= (p_j(x_i)) \in \mathbb{R}^{N\times Q}, \\ f_X &= (f(x_1), \dots, f(x_N))^T. \end{aligned} \tag{2.3}$$

From definition, the matrix A is symmetric and positive definite on the null space of P^T. We also assume that $N \geqslant Q$ and X is $\mathbb{P}_m^d$-unisolvent set to guarantee the solvability of system (2.2). For a (strictly) positive definite RBF, the symmetric matrix A is positive definite and the interpolation problem is solvable in the absence of polynomial terms.

An important class of RBFs that will be used in this paper is *polyharmonic splines* (PHS)

$$\phi_{d,k}(r) := \begin{cases} r^{2k-d}\log r, & k \in \mathbb{N},\ d \text{ even} \\ r^{2k-d}, & k \in \mathbb{N},\ d \text{ odd} \end{cases} \tag{2.4}$$

for $2k - d > 0$. The PHS function $\phi_{d,k}$ is (up to a sign) conditionally positive definite of order $m + 1 = k - \lceil d/2 \rceil + 1$. The *native space* associated to this RBF is the Beppo-Levi space

$$\mathrm{BL}_k(\mathbb{R}^d) := \{f \in C(\mathbb{R}^d) : D^\alpha f \in L_2(\mathbb{R}^d),\ \forall \alpha \in \mathbb{N}_0^d \text{ with } |\alpha| = k\}$$

provided that it is considered as a conditionally positive definite kernel of order k. Note that a conditionally positive definite function with respect to a polynomial space of a certain order is also conditionally positive definite with respect to higher order polynomial spaces. We refer the reader to [9,53] for more details about (conditionally) positive definite functions and their approximation properties.

3. Finite volume method

In this section, we provide a brief description about finite volume method (FVM) for solving the scalar conservation law. For a more detailed explanation, interested readers are referred to [17,34,51].

3.1. The scalar conservation law

Consider a scalar conservation law on an open and bounded computational domain $\Omega \subset \mathbb{R}^d$ with an initial condition as follows

$$\frac{\partial u}{\partial t} + \nabla \cdot F(u) = 0, \qquad u(0, x) = u_0(x). \tag{3.1}$$

Here, $F(u) := \left(f_1(u), \ldots, f_d(u)\right)^T$ is a *flux* function and $u \equiv u(t,x) : I \times \Omega \longrightarrow \mathbb{R}$ is the solution of the problem. Moreover, $I := \left(0, t_f\right]$ is a time interval with a final time t_f, and $u_0(x)$ is the initial function.

In order to discretize the problem (3.1) using FVM, we assume that the domain Ω is covered by a non-overlapping set of volumes (cells) $\left\{V_1, V_2, \ldots, V_N\right\} =: \mathcal{V}$. The integral form of the conservation law (3.1) on each volume $V \in \mathcal{V}$ at time $t \in I$ is obtained, after applying an integration by parts, as

$$\frac{d}{dt}\overline{u}_V + \frac{1}{|V|}\int_{\partial V} F(u)\cdot \nu \, \mathrm{d}s = 0, \qquad \text{for } V \in \mathcal{V}, \tag{3.2}$$

where

$$\overline{u}_V \equiv \overline{u}_V(t) := \frac{1}{|V|}\int_V u(t,x)\,\mathrm{d}x \qquad \text{for } V \in \mathcal{V},\ t \in I,$$

is the *cell average* value of u on volume V at time t. We assume that boundary of V is denoted by ∂V and composed of distinct segments $\Gamma_1, \ldots, \Gamma_q$, i.e., $\partial V = \cup_{j=1}^{q}\Gamma_j$. Also, ν is the unit outward normal vector to ∂V. Then, equation (3.2) can be rewritten as

$$\frac{d}{dt}\overline{u}_V + \frac{1}{|V|}\sum_{j=1}^{q}\int_{\Gamma_j} F(u(t,s))\cdot \nu_j \, \mathrm{d}s = 0, \tag{3.3}$$

where ν_j are normals to boundary segments Γ_j. The boundary integrals in (3.3) can be approximated by a n-point Gaussian quadrature (or else) to obtain

$$\frac{d}{dt}\overline{u}_V + \frac{1}{|V|}\sum_{j=1}^{q}\sum_{k=1}^{n}\omega_{j,k}F(u(t,z_{j,k}))\cdot \nu_j \approx 0, \tag{3.4}$$

where $\omega_{j,k}$ and $z_{j,k}$ for $k = 1, \ldots, n$ are integration weights and integration points, respectively, on interface Γ_j.

The next step replaces the exact flux $F(u)\cdot\nu$ by a numerical flux function $\widetilde{F}(u^+, u^-; \nu)$ in order to couple the subproblems defined on each FVM cells, and to ensure that information in the problem travels in the direction of the characteristic curves of the equation. Here, u^+ and u^- are solutions on the boundary ∂V from inside and outside, respectively. From the list of available numerical fluxes, this paper employs the *Lax-Friedrichs* numerical flux function [33,34]

$$\widetilde{F}(u^+, u^-; \nu) = \frac{1}{2}\left(F(u^+) + F(u^-)\right)\cdot\nu + \frac{\sigma}{2}(u^+ - u^-)$$

where σ is the maximum local speed and is obtained by

$$\sigma = \max_{\min(u^+,u^-)\le u\le \max(u^+,u^-)} |F'(u)\cdot\nu_j|, \qquad F'(u) = \left[\frac{df_1}{du}, \ldots, \frac{df_d}{du}\right].$$

When substituted into (3.4), $u^+(\cdot, z_{j,k})$ represents the solution at integration point $z_{j,k}$ within volume V itself, whereas $u^-(\cdot, z_{j,k})$ represents the solution at the same point, but obtaining from an adjacent volume that shares Γ_j as a common interface with volume V.

Finally, the cell average values $\{\overline{u}_V(t)\}_{V\in\mathcal{V}}$ are updated by solving the system of ODEs

$$\frac{d}{dt}\overline{u}_V(t) = L_V(\overline{u}_V(t)), \quad V \in \mathcal{V}, \tag{3.5}$$

where

$$L_V(\overline{u}_V(t)) = -\frac{1}{|V|}\sum_{j=1}^{q}\sum_{k=1}^{n}\omega_{j,k}\widetilde{F}(u^+(t,z_{j,k}), u^-(t,z_{j,k}); \nu_j). \tag{3.6}$$

Reconstructing u^+ and u^- from the current cell-averaged values $\{\overline{u}_V(t)\}_{V\in\mathcal{V}}$ is essential for updating the solution from time level t to the next time level $t + \Delta t$. Detailed explanations of some numerical methods for reconstruction will be provided later.

3.2. Time discretization

The system (3.5) can be integrated in time using an appropriate numerical ODE solver. The strong stability preserving (SSP) methods were originally developed for time integration in semi-discretizations of hyperbolic conservation laws [11–13,46]. In this paper, we employ the optimal third-order Shu-Osher SSP Runge-Kutta scheme [13,46]

$$\begin{aligned}
\overline{u}_V^{(1)} &= \overline{u}_V(t_j) + \Delta t L_V(\overline{u}_V(t_j)),\\
\overline{u}_V^{(2)} &= \frac{3}{4}\overline{u}_V(t_j) + \frac{1}{4}\overline{u}_V^{(1)} + \frac{1}{4}\Delta t L_V(\overline{u}_V^{(1)}),\\
\overline{u}_V(t_{j+1}) &= \frac{1}{3}\overline{u}_V(t_j) + \frac{2}{3}\overline{u}_V^{(2)} + \frac{2}{3}\Delta t L_V(\overline{u}_V^{(2)}),
\end{aligned}$$

to move from data $\{\bar{u}_V(t_j)\}_{V\in\mathcal{V}}$ at time $t_j = j\Delta t$ to data $\{\bar{u}_V(t_{j+1})\}_{V\in\mathcal{V}}$ at time t_{j+1}. The above three-stage third-order scheme is denoted by SSPRK(3,3). The global order of $(\Delta t)^3$ is achieved if the CFL condition

$$\Delta t \le \min_{V\in\mathcal{V}} \frac{r_V}{s_{\max}} \tag{3.7}$$

is satisfied [30,36]. Here r_V denotes the radius of the inscribed ball of volume V, and $s_{\max} = \max|F'(u)\cdot\nu|$, with the maximum taken over all integration points on the boundary of V. In cases where the order of spatial discretization exceeds three, we may choose to employ SSPRK(3,3) with a very smaller time step, or use the five-stage fourth-order scheme SSPRK(5,4) [11].

3.3. Reconstruction

In the reconstruction step, our goal is to approximate the density values u^+ and u^- in equation (3.6) (at integration points on cell interfaces) by reconstructing the function u from the cell average values $\{\bar{u}_V(t)\}_{V\in\mathcal{V}}$ at each time step. Reconstruction schemes are typically based on piecewise polynomials as seen in, for example, [34]. However, in this paper we explore a reconstruction method based on polyharmonic spline interpolation, as detailed in [2,3,23].

Suppose we have a fixed volume $V\in\mathcal{V}$, and consider its corresponding stencil

$$\mathcal{S} := \{C\}_{C\in\mathcal{S}} \subset \mathcal{V},$$

where $V\in\mathcal{S}$. Each cell $C\in\mathcal{S}$ is associated with a linear functional (cell average functional), represented as ℓ_C, defined as follows:

$$\ell_C(u) = \frac{1}{|C|}\int_C u(x)\,\mathrm{d}x, \quad \text{for all } C\in\mathcal{S},\ u(x)\equiv u(t,x). \tag{3.8}$$

To reconstruct cell averages $\{\ell_C\}$ within the stencil $\mathcal{S}$, we employ a generalized RBF interpolation method [53], which is expressed as

$$s(x) = \sum_{C\in\mathcal{S}} \alpha_C \ell_C^y \phi(\|x-y\|) + \sum_{j=1}^{Q} \beta_k p_j(x). \tag{3.9}$$

Here, ℓ_C^y denotes that the functional ℓ_C operates on the variable y of ϕ, i.e.,

$$\ell_C^y \phi(\|x-y\|) = \frac{1}{|C|}\int_C \phi(\|x-y\|)\,\mathrm{d}y, \quad C\in\mathcal{S}.$$

The coefficients α_C and β_j in (3.9) are determined by imposing the interpolation conditions

$$\ell_{C'}(u) = \ell_{C'}(s), \qquad \forall C'\in\mathcal{S},$$

along with the side condition

$$\sum_{C'\in\mathcal{S}} \alpha_{C'}\ell_{C'}(p_j) = 0, \quad j = 1,2,\dots,Q.$$

The interpolation conditions give

$$\ell_{C'}(u) = \ell_{C'}(s) = \sum_{C\in\mathcal{S}} \alpha_C \ell_{C'}^x \ell_C^y \phi(\|x-y\|) + \sum_{j=1}^{Q} \beta_k \ell_{C'}(p_j), \quad C, C'\in\mathcal{S}$$

which together with the side condition can equivalently be expressed as solving the system of linear equations

$$\begin{bmatrix} A_L & P_L \\ P_L^T & 0 \end{bmatrix}\begin{bmatrix} \alpha \\ \beta \end{bmatrix} = \begin{bmatrix} \ell_S \\ 0 \end{bmatrix}, \tag{3.10}$$

where

$$\begin{aligned} A_L &= (\ell_{C'}^x \ell_C^y \phi(\|x-y\|)), \quad C, C'\in\mathcal{S}, \\ P_L &= (\ell_C(p_j)), \quad C\in\mathcal{S},\ 1\leqslant j\leqslant Q, \\ \ell_S &= (\ell_C(u)), \quad C\in\mathcal{S}. \end{aligned} \tag{3.11}$$

To ensure a unique solution, the set $\{\ell_C\}_{C\in\mathcal{S}}$ must satisfy the property of being $\mathbb{P}_m^d$-unisolvent, meaning that if $\ell_C(p) = 0$ for all $C\in\mathcal{S}$, then $p\equiv 0$. In other words, any polynomial $p\in\mathbb{P}_m^d$ should be uniquely reconstructed from cell averages $\{\ell_C(p)\}_{C\in\mathcal{S}}$.

Nonetheless, a high-order reconstruction can lead to non-physical oscillations near discontinuities and shock fronts, and consequently can destabilize the solution.

3.4. WENO reconstruction

To suppress nonphysical oscillations near discontinuities and steep fronts, various techniques have been developed to enhance the reconstruction process [34]. In this section, we review the WENO reconstruction, which represents a weighted adaptation of the originally formulated ENO schemes. An ENO scheme was initially introduced in [16] for one-dimensional conservation laws. In the WENO reconstruction, first proposed in [35,27], a set of neighboring stencils $\{S_k,\ k = 1, \dots, K\}$ is selected for each control volume V, and in each stencil a reconstruction function is computed and weighted using an *oscillation indicator* that quantifies the smoothness of each function. Finally, the weighted (convex) combination of all K reconstructed functions is used as the ultimate reconstruction. In contrast, ENO schemes only utilize the smoothest reconstruction and discard the others. Different variants of ENO and WENO reconstructions have been developed and are frequently employed for solving various types of hyperbolic PDEs. For detailed examples refer to [45]. The authors of [2,3,23], employed the polyharmonic spline interpolation for reconstruction, as discussed in Section 3.3. They define the oscillation indicator $\mathcal{I}$ by

$$\mathcal{I}(s) = |s|_{\mathrm{BL}_k(\mathbb{R}^d)}, \quad s \in \mathrm{BL}_k(\mathbb{R}^d),$$

as the Beppo-Levi space $\mathrm{BL}_k(\mathbb{R}^d)$ is the optimal recovery space for polyharmonic splines [53]. A reconstructed function s_j (associated with stencil S_j) with a smaller $\mathcal{I}(s_j)$ is assumed to be smoother and should therefore receive a higher weight. They introduce intermediate values

$$\tilde{w}_j = \frac{1}{(\epsilon + \mathcal{I}(s_j))^\rho}, \quad j = 1, 2, \dots, K$$

for some $\epsilon, \rho > 0$, and then compute the final weights

$$w_j = \frac{\tilde{w}_j}{\sum_{i=1}^{K} \tilde{w}_i}, \quad j = 1, 2, \dots, K,$$

ensuring that $w_1 + \cdots + w_K = 1$. The WENO reconstruction is then defined as

$$s = w_1 s_1 + \cdots + w_K s_K.$$

To find other RBF-ENO/WENO reconstructions see [4,18,19,56], and to explore other variations involving different approximation techniques, refer to [5,25,26].

To render the WENO process applicable to a wide range of problems, the configuration and size of stencils are crucial and significantly impact the quality and accuracy of the reconstruction. Three types of such stencils are experimentally examined and introduced in [3].

4. Approximate interpolation and smoothing

Our approach to avoid nonphysical oscillations in the solution (see Section 5 below) is motivated by *approximate interpolation* on scattered data points. Let us consider N centers $X = \{x_1, \dots, x_N\}$ distributed within the bounded region $\Omega \subset \mathbb{R}^d$, along with their corresponding values, $y_1, \dots, y_N \in \mathbb{R}$. We assume that these values are sampled from an unknown function $f \in C(\Omega)$ where $y_j = f(x_j)$ for $j = 1, \dots, N$. The aim is to find a function $s \in C(\Omega)$ that approximates the function f by utilizing the available values of f at X. In an interpolation process, the error function $f - s$ vanishes at point set X while in an approximation process, such as a curve fitting method, small errors at centers are admissible. When the data values are noisy or inaccurate, the second approach provides a better and smoother overall approximation. This process is referred to as approximate interpolation if we permit slight deviations from interpolation constraints to regularize the solution. This concept is related to *Tikhonov regularization* and *smoothing splines* in the context of approximation theory [40].

Suppose $\mathcal{H} \subset C(\Omega)$ is a normed linear space of continuous functions. Also, assume that $\mathcal{G}$ is another normed linear space, and $T : \mathcal{H} \to \mathcal{G}$ is a linear mapping. If $J : \mathcal{H} \to \mathbb{R}$ is defined as $J(s) = |Ts|$, then for the given data sites $X = \{x_1, \dots, x_N\}$ and their corresponding values $f(x_1), \dots, f(x_N) \in \mathbb{R}$, the smoothing spline $s_\lambda \in \mathcal{H}$ is defined as the solution of the following minimization problem:

$$\min \left\{ \sum_{j=1}^{N} [f(x_j) - s(x_j)]^2 + \lambda J(s) : s \in \mathcal{H} \right\}, \tag{4.1}$$

where $\lambda \geqslant 0$ is a smoothing parameter. If λ gets smaller toward zero, then (4.1) tends to be an interpolation problem. Too large values of λ, on the other hand, violate the interpolation conditions and result in a solution which might smear out the data too much. Thus, determining a proper value for this parameter is a challenging task.

Duchon [8] (see also Wendland and Rieger [54]) considered the smoothing spline problem using polyharmonic splines $\phi_{d,k}(\|x\|)$, $x \in \mathbb{R}^d$. The approximation space $\mathcal{H}$ is assumed to be the Beppo-Levi space

$$\mathcal{H} = \mathrm{BL}_k(\mathbb{R}^d), \quad k > 2d,$$

and the functional J on this space is defined as

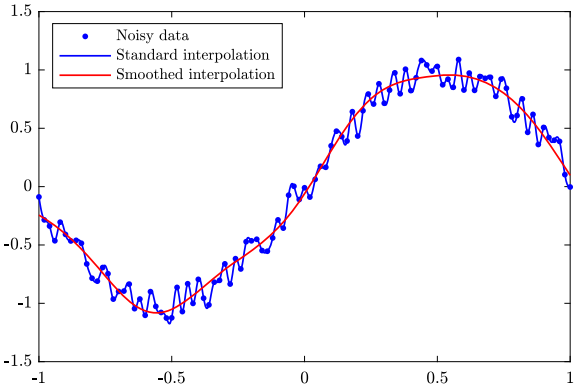

Fig. 1. Standard PHS interpolation vs. the smoothed PHS interpolation. (For interpretation of the colors in the figure(s), the reader is referred to the web version of this article.)

$$J(f) := |f|^2_{\mathrm{BL}_k(\mathbb{R}^d)}.$$

The solution of the minimization problem is then given by

$$s(x) = \sum_{j=1}^{N} \alpha_j \phi_{d,k}(\|x - x_j\|) + \sum_{j=1}^{Q} \beta_j p_j(x) \tag{4.2}$$

where $\phi_{d,k}$ is the PHS kernel (2.4), $\{p_1, \dots, p_Q\}$ is a basis for polynomial space $\mathbb{P}^d_{k-1}$, and the coefficients α_j and β_j solve the linear system of equations

$$\begin{bmatrix} A + \lambda I & P \\ P^T & 0 \end{bmatrix} \begin{bmatrix} \alpha \\ \beta \end{bmatrix} = \begin{bmatrix} f_X \\ 0 \end{bmatrix} \tag{4.3}$$

provided that X is a $\mathbb{P}^d_{k-1}$-unisolvent set. Here, $\phi_{d,k}$ is considered to be conditionally positive definite of order k instead of $k - \lceil d/2 \rceil + 1$. The matrix I is the identity matrix of size N. The proof for a generalized form of this problem is given in Theorem 4.2 below.

The difference between the approximate interpolation system in (4.3) and the pure interpolation in (2.2) is a diagonal increment with λ, causing the interpolant to pass close to interpolation points (if λ is small) but not exactly through them. For a given set of noisy data, this leads to a smooth (non-oscillatory) approximation. See Fig. 1. However, this type of smoothing is not appropriate for suppressing the oscillations near discontinuities in the FVM setting.

In this paper, we introduce a more general approximate interpolation problem that allows different weights for different interpolation points:

$$\min \left\{ \sum_{j=1}^{N} \frac{1}{\lambda_j} [f(x_j) - s(x_j)]^2 + |f|^2_{\mathrm{BL}_k(\mathbb{R}^d)} : s \in \mathrm{BL}_k(\mathbb{R}^d) \right\}, \tag{4.4}$$

where λ is replaced by N given smoothing parameters $\lambda_j > 0$, each corresponding to interpolation point x_j for $j = 1, \dots, N$. To obtain the form of the solution of this problem we need the following result.

Lemma 4.1. *Assume that $\mathcal{N}_\phi$ is the native space corresponding to conditionally positive definite kernel ϕ with respect to polynomial space $\mathbb{P}^d_m = \mathrm{span}\{p_1, \dots, p_Q\}$. For a given $\mathbb{P}^d_m$-unisolvent set $X = \{x_1, \dots, x_N\} \subset \Omega$, assume that $P = (p_j(x_i)) \in \mathbb{R}^{N \times Q}$, and $H_{\phi,X}$ is a finite dimensional space of the form*

$$H_{\phi,X} := \left\{ \sum_{j=1}^{N} \alpha_j \phi(\|\cdot - x_j\|) : \alpha \in \mathbb{R}^N \text{ with } P^T \alpha = 0 \right\}.$$

Moreover, assume that $\mathcal{R}$ is the orthogonal complement of subspace $H_{\phi,X} + \mathbb{P}^d_m$ of $\mathcal{N}_\phi$. Then for every function $v \in \mathcal{R}$ the vector $v_X = (v(x_1), \dots, v(x_N))^T$ is perpendicular to the null space of P^T, i.e., $v_X^T \alpha = 0$ provided that $P^T \alpha = 0$.

Proof. According to definition of space $H_{\phi,X}$, every function $w \in H_{\phi,X} + \mathbb{P}^d_m$ can be written as $w = \mu^x \phi(\|\cdot - x\|) + q$ with $q \in \mathbb{P}^d_m$ and a certain linear functional

$$\mu = \sum_{j=1}^{N} \alpha_j \delta_{x_j}$$

for some coefficients α_j with $\mu(p)=0$ for all $p\in\mathbb{P}_m^d$. Here, δ_x is the point evaluation functional; $\delta_x f := f(x)$. The superscript x on functional μ^x means that μ acts on variable x of $\phi(\|y-x\|)$. Consider a set of $\mathbb{P}_m^d$-unisolvent points $E=\{\xi_1,\dots,\xi_Q\}\subset\Omega$ and assume that $\Pi:\mathcal{N}_\phi\to\mathbb{P}_m^d$ is the polynomial interpolation operator on centers E. Also assume that $G(\cdot,x)=\phi(\|\cdot-x\|)-\Pi^x\phi(\|\cdot-x\|)$, the pointwise polynomial interpolation error of basis function ϕ with respect to the second argument. Now, for a function v in $\mathcal{R}$ we have

$$\begin{aligned}0&=\langle v,w\rangle_{\mathcal{N}_\phi}\\&=\langle v,\mu^x\phi(\|\cdot-x\|)+q\rangle_{\mathcal{N}_\phi}\\&=\langle v,\mu^x\phi(\|\cdot-x\|)\rangle_{\mathcal{N}_\phi}\\&=\mu(\Pi v)+\langle v,\mu^x G(\cdot,x)\rangle_{\mathcal{N}_\phi}\\&=\mu(v)=\sum_{j=1}^N\alpha_j v(x_j)\end{aligned}$$

for every function $w\in H_{\phi,X}+\mathbb{P}_m^d$. The third equality holds true because $\langle v,q\rangle_{\mathcal{N}_\phi}=0$. For the fourth and fifth equalities we use the fact that $\mu(\Pi v)=0$, and Theorem 10.17 of [53]. This means that for every vector α in the null space of P^T we have

$$\sum_{j=1}^N\alpha_j v(x_j)=0.\quad\square$$

Theorem 4.2. *The solution of problem* (4.4) *is given by* (4.2) *where* α *and* β *satisfy the following system of equations*

$$\begin{bmatrix}A+\Lambda & P\\ P^T & 0\end{bmatrix}\begin{bmatrix}\alpha\\ \beta\end{bmatrix}=\begin{bmatrix}f_X\\ 0\end{bmatrix}\tag{4.5}$$

for $\Lambda=\operatorname{diag}\{\lambda_1,\dots,\lambda_N\}$. *Here,* A, P, *and* f_X *are defined as* (2.3) *for* $\phi=\phi_{d,k}$ *and* $m=k-1$.

Proof. The native space corresponding to kernel $\phi_{d,k}$ is known to be the Beppo-Levi space $\mathrm{BL}_k(\mathbb{R}^d)$, and $H_{\phi_{d,k},X}+\mathbb{P}_m^d$ is a subspace of the native space [53, Chapter 10]. Every function $s\in\mathrm{BL}_k(\mathbb{R}^d)$ can be written as $s=w+v$ where $w\in H_{\phi_{d,k},X}+\mathbb{P}_m^d$ and v is some element in $\mathcal{R}\subset\mathrm{BL}_k(\mathbb{R}^d)$, the orthogonal complement of subspace $H_{\phi_{d,k},X}+\mathbb{P}_m^d$. In fact,

$$w=\sum_{j=1}^N\alpha_j\phi(\|\cdot-x_j\|)+\sum_{j=1}^Q\beta_j p_j$$

for some vectors $\alpha\in\mathbb{R}^N$ and $\beta\in\mathbb{R}^Q$ with $P^T\alpha=0$, and $v\in\mathcal{R}$. It is known that the native space semi-norm of w is $\alpha^T A\alpha$ as the norm of polynomials in $\mathbb{P}_m^d$ is zero [53, Chapter 10]. This means that

$$|s|^2_{\mathrm{BL}_k(\mathbb{R}^d)}=\alpha^T A\alpha+|v|^2_{\mathrm{BL}_k(\mathbb{R}^d)}.$$

Using these, the target function of minimization problem (4.4) can be reformulated as

$$T(\alpha,\beta,v):=\left[f_X-(A\alpha+P\beta+v_X)\right]^T\Lambda^{-1}\left[f_X-(A\alpha+P\beta+v_X)\right]+\alpha^T A\alpha+|v|^2_{\mathrm{BL}_k(\mathbb{R}^d)}$$

which must be minimized over all $[\alpha^T\ \beta^T]\in\mathbb{R}^{N+Q}$ with $P^T\alpha=0$ and all $v\in\mathcal{R}$. First, for a given $v\in\mathcal{R}$ we minimize $T(\alpha,\beta,v)$ over all $[\alpha^T\ \beta^T]\in\mathbb{R}^{N+Q}$ with $P^T\alpha=0$. This is a quadratic optimization problem as the target function $T(\alpha,\beta,v)$ can be rewritten as

$$\begin{aligned}T(\alpha,\beta,v)=&[\alpha^T\ \beta^T]\begin{bmatrix}A\Lambda^{-1}A+A & A\Lambda^{-1}P\\ P^T\Lambda^{-1}A & P^T\Lambda^{-1}P\end{bmatrix}\begin{bmatrix}\alpha\\ \beta\end{bmatrix}\\&-2[\alpha^T\ \beta^T]\begin{bmatrix}A\Lambda^{-1}(f_X-v_X)\\ P^T\Lambda^{-1}(f_X-v_X)\end{bmatrix}+(f_X-v_X)^T\Lambda^{-1}(f_X-v_X)+|v|^2_{\mathrm{BL}_k(\mathbb{R}^d)}.\end{aligned}$$

Since A is positive definite on the null space of P^T, the block matrix is positive definite, and the unique solution of the minimization problem satisfies

$$\begin{bmatrix}A\Lambda^{-1}A+A & A\Lambda^{-1}P\\ P^T\Lambda^{-1}A & P^T\Lambda^{-1}P\end{bmatrix}\begin{bmatrix}\alpha\\ \beta\end{bmatrix}=\begin{bmatrix}A\Lambda^{-1}(f_X-v_X)\\ P^T\Lambda^{-1}(f_X-v_X)\end{bmatrix}$$

or

$$\begin{bmatrix}A\Lambda^{-1} & 0\\ P^T\Lambda^{-1} & -I\end{bmatrix}\begin{bmatrix}A+\Lambda & P\\ P^T & 0\end{bmatrix}\begin{bmatrix}\alpha\\ \beta\end{bmatrix}=\begin{bmatrix}A\Lambda^{-1} & 0\\ P^T\Lambda^{-1} & -I\end{bmatrix}\begin{bmatrix}f_X-v_X\\ 0\end{bmatrix}$$

which is equivalent to

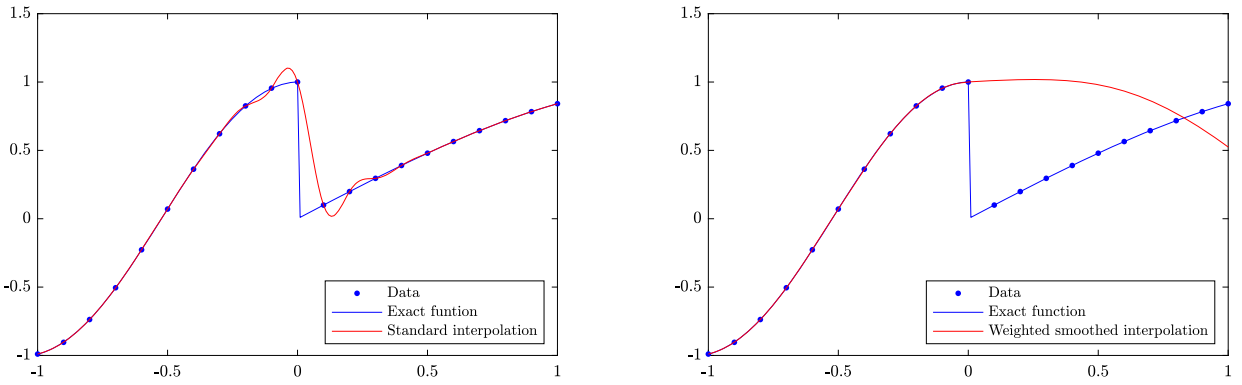

Fig. 2. Standard PHS interpolation (left) vs. the generalized smoothed PHS interpolation (right) for a discontinuous 1D function.

$$\begin{bmatrix} A+\Lambda & P \\ P^T & 0 \end{bmatrix} \begin{bmatrix} \alpha \\ \beta \end{bmatrix} = \begin{bmatrix} f_X - v_X \\ 0 \end{bmatrix} \tag{4.6}$$

as the premultiplied matrix is non-singular on the null space of P^T. Note that the linear system (4.6) is non-singular because P is full-rank and $A+\Lambda$ is positive definite on the null space of P^T (since A has this property and Λ is non-negative). The target function evaluated at optimal vectors α and β becomes (as a function of v)

$$\begin{aligned} T(\alpha,\beta,v) &= \alpha^T(A+\Lambda)\alpha + |v|^2_{\mathrm{BL}_k(\mathbb{R}^d)} \\ &= \alpha^T(f_X - v_X) + |v|^2_{\mathrm{BL}_k(\mathbb{R}^d)} \\ &= \alpha^T f_X + |v|^2_{\mathrm{BL}_k(\mathbb{R}^d)}. \end{aligned}$$

In the final equality we have used $\alpha^T v_X = 0$ from Lemma 4.1. The optimal solution is clearly obtained at $v = 0$, also rendering (4.6) equivalent to (4.5). □

In the setting given above, the polyharmonic kernel $\phi_{d,k}$ can be replaced by other (conditionally) positive definite functions. In this case, the space $\mathcal{H}$ and functional J are replaced by the native space of the new kernel and the (semi-) norm defined on the native space, respectively.

In Fig. 2, the standard and generalized smoothing interpolations are plotted for a discontinuous 1D function. When we prioritize the accuracy of the approximation on the left side of the discontinuity, with no emphasis on the right side, the generalized smoothing approach is an appropriate choice. A comparable scenario arises in transport equations when waves propagate either to the right or left side, requiring a careful selection of either a backward or forward stencil to guarantee the stability of solution.

In the sequel, we will use an extended and localized version of the above generalized smoothing interpolation problem to reconstruct function values on cell boundaries from cell averages in the course of the FVM algorithm for conservation laws.

5. FVM with weighted smoothed reconstruction

As previously described, the central idea behind WENO reconstruction technique is to employ one-sided stencils in regions of the domain where the solution function changes rapidly or contains discontinuities and shocks. This process involves creating different stencils for each volume, interpolating within each of these stencils, calculating the oscillation indicator of each interpolant, and finally determining a weighted interpolation. In this section, we propose an alternative technique based on a tricky smoothing approach that employs only one central stencil, even in regions with high gradients or discontinuities. The new method suppresses the oscillations by degrading the impact of unfitted interpolation points. This approach is built upon the generalized smoothing technique we introduced in Section 4.

5.1. Reconstruction from cell averages using WSR

The smoothing spline problem (4.4) can be extended to the more general setting

$$\min\left\{ \sum_{j=1}^{N} \frac{1}{\lambda_j} [\ell_j(f) - \ell_j(s)]^2 + |f|^2_{\mathrm{BL}_k(\mathbb{R}^d)} : s \in \mathrm{BL}_k(\mathbb{R}^d) \right\}, \tag{5.1}$$

where ℓ_j, $j = 1,\dots,N$ are N linearly independent functionals from $\mathrm{BL}_k^*(\mathbb{R}^d)$, the dual space of $\mathrm{BL}_k(\mathbb{R}^d)$, with the property that $\ell_j(p) = 0$ for all $j = 1,\dots,N$ and $p \in \mathbb{P}^d_m$ implies that $p = 0$. The same proof shows that the solution of (5.1) is of the form

$$s(x) = \sum_{j=1}^{N} \alpha_j \ell_j^y \phi_{d,k}(\|x-y\|) + \sum_{j=1}^{Q} \beta_j p_j(x)$$

where α and β satisfy the following system of equations

$$\begin{bmatrix} A_L + \Lambda & P_L \\ P_L^T & 0 \end{bmatrix} \begin{bmatrix} \alpha \\ \beta \end{bmatrix} = \begin{bmatrix} \ell(f) \\ 0 \end{bmatrix}$$

where $\Lambda = \mathrm{diag}\{\lambda_1, \dots, \lambda_N\}$, and A, P, and $\ell(f)$ are defined as

$$A_L = (\ell_i^x \ell_j^y \phi(\|x-y\|)), \quad i,j = 1,\dots,N,$$
$$P_L = (\ell_j(p_i)), \quad j = 1,\dots,N,\ i = 1,\dots,Q,$$
$$\ell(f) = (\ell_1(f), \dots, \ell_N(f))^T.$$

To apply this approximation on FV stencils, consider a specific volume V and a central stencil $\mathcal{S}$ around it. Define the cell average functionals $\{\ell_C : C \in \mathcal{S}\}$ as (3.8), and for the purpose of reconstruction from these cell averages, employ the smoothing problem (5.1) with $f = u$, $N = |\mathcal{S}|$ (number of cells in $\mathcal{S}$), $\ell_j = \ell_C$, and $\lambda_j = \lambda_C$ for $C \in \mathcal{S}$. The reconstructed function then has the form

$$s(x) = \sum_{C \in \mathcal{S}} \alpha_C \ell_C^y \phi_{d,k}(\|x-y\|) + \sum_{j=1}^{Q} \beta_j p_j(x),$$

where the coefficients α and β satisfy the linear system

$$\begin{bmatrix} A_L + \Lambda & P_L \\ P_L^T & 0 \end{bmatrix} \begin{bmatrix} \alpha \\ \beta \end{bmatrix} = \begin{bmatrix} \ell_{\mathcal{S}} \\ 0 \end{bmatrix} \tag{5.2}$$

where

$$\Lambda = \mathrm{diag}\{\lambda_C\}_{C \in \mathcal{S}}, \tag{5.3}$$

and A_L, P_L and $\ell_{\mathcal{S}}$ are defined as (3.11). Furthermore, we assume that

$$\lambda_C = \psi(u; C; \mathcal{S}), \quad C \in \mathcal{S}$$

where ψ is a suitable *nonnegative* function that depends on the solution function u and all cells in the stencil $\mathcal{S}$. This function should be chosen such that it gives higher weights to more important cells and lower weights to the others. We apply the following criterion:

The closer the values of the average of function u on cells in stencil $\mathcal{S}$ are to its average value on the central stencil V, the smaller the smoothing parameters associated with these cells become, thereby granting them greater importance. In this paper, we use the function

$$\lambda_C = \psi(u; C, \mathcal{S}) = |\overline{u}_V - \overline{u}_C|^\eta, \quad C \in \mathcal{S},\ \eta \geq 1, \tag{5.4}$$

as a model for this criterion. See subsection 5.4 below. This process is referred to as *weighted smoothed reconstruction* (WSR) and yields a smooth approximation around the cell V within the stencil $\mathcal{S}$ where the function f has a discontinuity or a steep gradient. The approximate interpolation obtained from WSR can be employed to compute the numerical flux along the boundaries of volume V. The remaining steps of the classical FVM are executed as usual. This new scheme is abbreviated as FVM-WSR.

We note that the WSR method can use not only the polyharmonic spline kernels but also other radial basis functions and various types of approximation functions such as polynomials. However, in this paper, our focus is primarily on polyharmonic splines.

5.2. About conditioning of local systems

The issue of ill-conditioning arises in the PHS reconstruction when dealing with small meshsizes to set up the system (5.2). To overcome this problem, one can solve the generalized interpolation problem (5.2) on a blown-up stencil $\hat{\mathcal{S}}$ by *scaling* the original stencil $\mathcal{S}$. Out of all the well-known RBFs, this technique is only applicable to PHS kernels (2.4) [7,22,37]. In our setting with special functionals ℓ_C we use a method similar to the one described in [29]. Consider the weighted smoothed approximation $s(x)$ on the stencil $\mathcal{S} = \{C\}_{C \in \mathcal{S}}$ corresponding to the volume $V \in \mathcal{V}$. To perform this reconstruction on a scaled stencil, we use the mapping

$$T_V(x) := \frac{x - b_V}{h} : \mathcal{S} \longrightarrow \hat{\mathcal{S}}$$

where b_V is the barycenter of volume V, and h is the meshsize. Then we can show that the weighted smoothed approximation on the new shifted and scaled stencil $\hat{\mathcal{S}} = \{\hat{C} = T_V(C) : C \in \mathcal{S}\}$ is equivalent to the original approximation, i.e.,

$$s(x) = \sum_{\hat{C} \in \hat{\mathcal{S}}} \hat{\alpha}_{\hat{C}} \ell_{\hat{C}}^{\hat{y}} \phi(\|\hat{x} - \hat{y}\|) + \sum_{j=1}^{Q} \hat{\beta}_j p_j(\hat{x}),$$

where $\hat{x} = T_V(x)$ and the coefficients $\hat{\alpha}$ and $\hat{\beta}$ satisfy the linear system

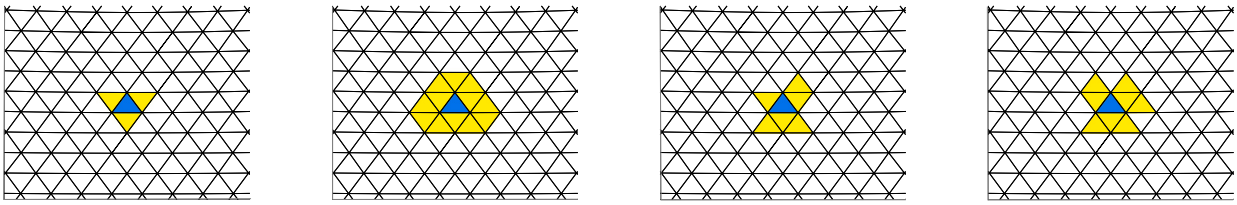

Fig. 3. The blue triangle stands for central triangle V, and the yellow triangles form a central stencil for V. From left to right: the $S_N(V)$ stencil, the $S_M(V)$ stencil, a subset of $S_M(V)$ of size 7, a subset of $S_M(V)$ of size 9.

$$\begin{bmatrix} \hat{A}_L + \hat{\Lambda} & \hat{P}_L \\ \hat{P}_L^T & 0 \end{bmatrix} \begin{bmatrix} \hat{\alpha} \\ \hat{\beta} \end{bmatrix} = \begin{bmatrix} \ell_S \\ 0 \end{bmatrix}$$

for

$$\hat{\Lambda} = h^{-2k+d}\Lambda,$$

where $2k - d$ is the exponent of the polyharmonic kernel (2.4), and

$$\hat{A}_L = (\ell_{\hat{C}}^x \ell_{\hat{C}'}^y \phi(\|x - y\|)), \quad \hat{C}, \hat{C}' \in \hat{S},$$
$$\hat{P}_L = (\ell_{\hat{C}}(p_j)), \quad \hat{C} \in \hat{S},\ 1 \leqslant j \leqslant Q,$$
$$\ell_S = (\ell_C(u)), \quad C \in S.$$

The proof closely follows that given in [29, Chapter 3] with a slight modification for additional matrix Λ in the coefficient matrix of linear system (5.2). This matrix needs to be replaced by $\hat{\Lambda}$ in the scaled version. The matrices $\hat{A}_L$ and $\hat{P}_L$ are now independent of the mesh parameter h, and if we appropriately scale the matrix Λ, the condition number of the scaled system remains constant, independent of h. For example, if the smoothing parameters λ_C are chosen as (5.4) then $\Lambda = \tilde{\Lambda} \cdot \mathcal{O}(h^\eta)$ where $\tilde{\Lambda}$ depends on the gradient of u and is independent of h. Therefore, scaling Λ by $h^{2k-d-\eta}$ renders $\hat{\Lambda}$ independent of h and results in an h-independent condition number for the entire system. However, this scaling of Λ may not always yield the most accurate results. If the user opts for a different scaling, the contribution of $\hat{\Lambda}$ may lead to some worse condition numbers for very small values of h. In such cases, the adaptation of preconditioning techniques for saddle point systems would be helpful, although this aspect has not been addressed in this work.

5.3. Central stencils

In this paper, we use a conforming triangulation to form the volumes. A requirement for applying polyharmonic spline RBFs in the reconstruction step of FVM-WSR is that the stencil size matches or exceeds the associated polynomial space dimension. In the experimental section we employ polyharmonic splines $\phi_{2,2}(r) = r^2 \log(r)$, $\phi_{2,3}(r) = r^4 \log(r)$ and $\phi_{2,4}(r) = r^6 \log(r)$. The polynomial space dimensions associated with these kernels in the two-dimensional space are 3, 6 and 10, respectively. We address how a central stencil can be formed to fulfill the solvability requirement and yield the expected accuracy.

For a given volume (triangle) V, the Neumann neighborhood of V is denoted by $S_N(V)$ and includes all triangles that share an edge with V. On the other hand, the Moore neighborhood of V is denoted by $S_M(V)$ and includes all triangles that share an edge or a vertex with V. It is clear that $S_N(V) \subset S_M(V)$. The Moore neighborhood is usually well distributed in all directions around the central volume V. Experimental results showed that the optimal stencil size for WSR depends on the smoothness of the solution: smaller stencils are preferable for smooth solutions, while larger stencils are needed for solutions with discontinuities or steep gradients. We may use a subset of $S_M(V)$ with certain number of triangles for different types of RBFs. In Fig. 3 some stencils are depicted for a sample triangle V (the blue triangle).

5.4. Smoothing parameters

The choice of smoothing parameters in (5.3) requires some consideration to achieve an approximation with minimal oscillation and optimal rate of convergence. This choice depends on the behavior of the solution within the stencil where we intend to reconstruct the function. As previously explained, the value of λ_C inversely correlates with the influence of volume C on the weighted approximation. For instance, volume V holds the highest influence as $\lambda_V = 0$. When a discontinuity traverses through a stencil, sharp differences between cell averages within that stencil can arise. To address this, the smoothing function should assign a small λ_C (resulting in a large weight) to a cell C whose cell average closely aligns with that of volume V. Conversely, cells with cell averages significantly different from that of V should be assigned a large λ_C (resulting in a small weight). To model such a behavior, we employ the expression (5.4) for λ_C values, although the user can design other possible formulations. See Fig. 4 for different powers η.

Our experiments show that using a power value of $\eta = 3$ yields accurate and less oscillatory solutions for problems with both smooth and discontinuities (and shock front) solutions. However, for problems with smooth solutions specifically, using a power

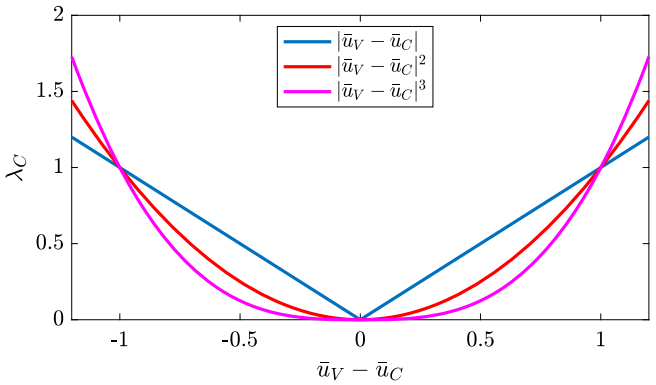

Fig. 4. A model for the smoothing function.

value of η between 1 and 2 results in convergence orders that are closer to the expected theoretical orders. To introduce adaptability into this approach for problems with discontinuous and shock solutions, we follow this procedure:

1. Calculate $\bar{u}_{max} = \max_{C \in S}\{|\ell_C(u)|\}$ and $\bar{u}_{min} = \min_{C \in S}\{|\ell_C(u)|\}$,
2. Compute $p = (\bar{u}_{max} - \bar{u}_{min})/(h\sqrt{|S|})$,
3. If $p < K$, set $\eta = 2$; otherwise, set $\eta = 3$.

Here, $|S|$ represents the size of stencil, h denotes the meshsize, and K is a user-defined constant. For our experiments, we have chosen $K = 2$.

6. Experimental results

In this section, we apply FVM-WSR to both linear and nonlinear conservation law equations with smooth and discontinuous initial conditions. We compare errors with those obtained using FVM-WENO. For temporal discretization, we employ SSPRK(3,3) in all examples except for one case, in which we use SSPRK(5,4). The code is implemented in MATLAB and executed on a machine equipped with a Core(TM) i7-6700k CPU running at 4 GHz, and 16 GB of RAM.

Since all experiments are provided for two-dimensional hyperbolic PDEs, we employ the notation $x = (x_1, x_2)$ to denote a point in $\mathbb{R}^2$. We have also implemented the method for various 1D conservation laws and obtained the expected results. However, in the interest of brevity and to control the length of paper, we do not include them here. Instead, we focus on presenting 2D problems exclusively.

In the reconstruction step, we utilize the PHS kernels $\phi_{2,2}(r) = r^2 \log(r)$ (2nd order), $\phi_{2,3}(r) = r^4 \log(r)$ (3rd order), and $\phi_{2,4}(r) = r^6 \log(r)$ (4th order), each with central stencils of sizes 7, 9, and 15, respectively. For the highest-order RBF, we employ SSPRK(5,4) for time discretization while we use SSPRK(3,3) for the others. In all cases, the steplength Δt is chosen small enough to satisfy the CFL condition (3.7) on all stencils.

6.1. Linear advection with a smooth initial condition

Consider the linear advection equation

$$u_t + u_{x_1} + u_{x_2} = 0, \tag{6.1}$$

where $u := u(t,x) : [0, t_f] \times [-0.5, 0.5]^2 \longrightarrow \mathbb{R}$, with periodic boundary conditions. We apply the initial condition:

$$u(0,x) = \sin^2\left(\pi\left(x_1 + \frac{1}{2}\right)\right)\sin^2\left(\pi\left(x_2 + \frac{1}{2}\right)\right), \tag{6.2}$$

as depicted in the top-left of Fig. 5. As time advances, the exact solution of (6.1) propagates in the direction $[1,1]$ and retains its initial shape in an extended domain at $t = 1$.

Table 2 presents the norm-1 and norm-infinity errors at the final time $t = 1$ for both WSR and WENO methods. The results are obtained on a sequence of triangulations with meshsizes $h = \frac{1}{8}, \frac{1}{16}, \frac{1}{32}, \frac{1}{64}$, and $\frac{1}{128}$. The steplength Δt is initially set to 0.02 for $h = \frac{1}{8}$ and is halved successively as the values of h are divided by 2. As shown, FVM with WSR achieves (approximately) the expected convergence orders in norm-1 and norm-infinity (also in norm 2, though not reported in the table), except for the norm infinity of the 4th order scheme, where the order appears to stay about 3.2. However, the experiment demonstrates a superior convergence compared to the WENO scheme. The results of the WENO method depend on the selection of forward and backward stencils where different choices may yield more or less accurate solutions. In this study, we follow the criteria outlined in [3] for our selection

Table 2
The ℓ_1-norm and ℓ_∞ errors (L1E and InfE) and orders of convergence for the numerical solutions of the advection equation (6.1) with initial condition (6.2) at $t = 1$ using FVM-WSR and FVM-WENO, with polyharmonic spline RBFs $r^2 \log r$ (2nd order), $r^4 \log r$ (3rd order), and $r^6 \log r$ (4th order).

	h	2nd order				3rd order				4th order			
		L1E	q	InfE	q	L1E	q	InfE	q	L1E	q	InfE	q
	1/8	3.05e − 2	–	1.17e − 1	–	2.14e − 2	–	6.80e − 2	–	4.21e − 3	–	2.17e − 2	–
W	1/16	7.11e − 3	2.10	3.57e − 2	1.71	3.28e − 3	2.70	1.11e − 2	2.61	4.24e − 4	3.31	2.74e − 3	2.98
S	1/32	1.94e − 3	1.87	8.59e − 3	2.06	4.53e − 4	2.86	1.43e − 3	2.96	2.80e − 5	3.92	3.04e − 4	3.17
R	1/64	5.37e − 4	1.85	3.17e − 3	1.44	5.82e − 5	2.96	1.85e − 4	2.94	2.01e − 6	3.79	3.17e − 5	3.26
	1/128	1.40e − 4	1.94	7.46e − 4	2.09	7.39e − 6	2.98	2.55e − 5	2.86	1.37e − 7	3.88	3.42e − 6	3.21
W	1/8	3.02e − 2	–	9.41e − 2	–	2.05e − 2	–	6.73e − 2	–	–	–	–	–
E	1/16	8.79e − 3	1.78	3.12e − 2	1.59	6.22e − 3	1.72	2.11e − 2	1.67	–	–	–	–
N	1/32	2.33e − 3	1.91	9.69e − 3	1.69	1.15e − 3	2.43	6.02e − 3	1.81	–	–	–	–
O	1/64	6.96e − 4	1.74	4.02e − 3	1.27	2.14e − 4	2.42	1.21e − 3	2.31	–	–	–	–
	1/128	2.18e − 4	1.68	1.25e − 3	1.69	4.45e − 5	2.27	3.29e − 4	1.88	–	–	–	–

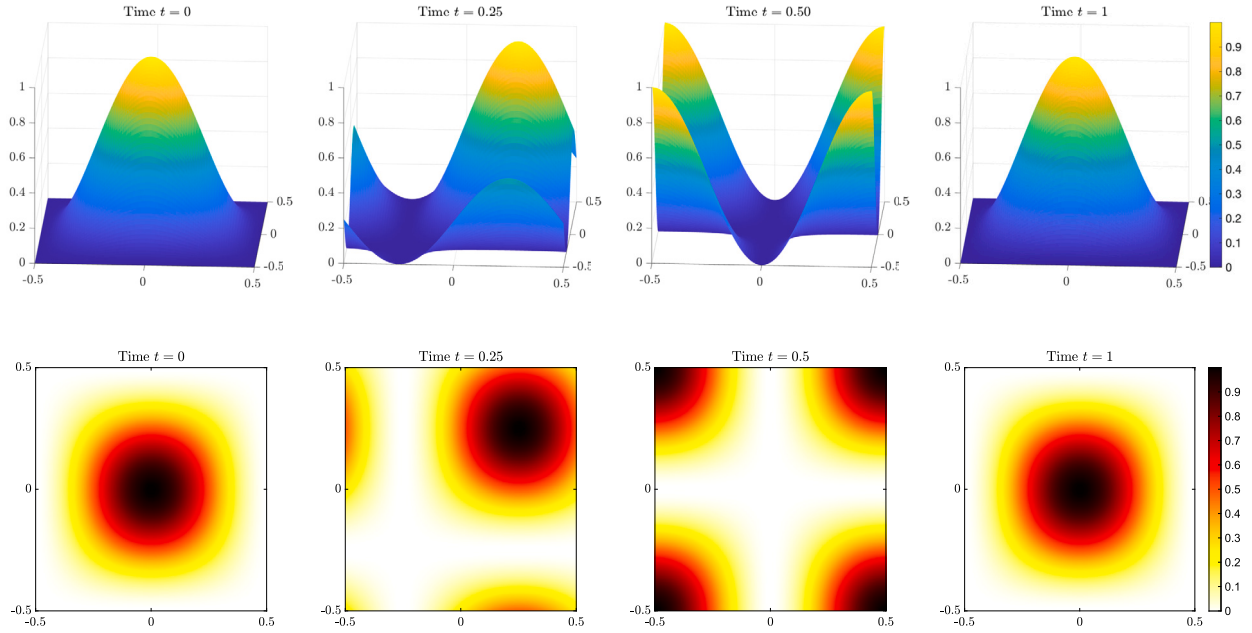

Fig. 5. The initial condition (6.2) and numerical solutions using FVM-WSR for the advection equation at time levels $t = 0.25$, $t = 0.5$, and $t = 1$.

Table 3
Runtime comparison: FVM-WSR vs. FVM-WENO.

h	$\frac{1}{8}$	$\frac{1}{16}$	$\frac{1}{32}$	$\frac{1}{64}$	$\frac{1}{128}$
$\frac{\text{WENO}}{\text{WSR}}$	2.25	2.24	2.12	1.97	1.84

process. However, as there is no reported selection criterion for a 4th order RBF-based method in the mentioned reference or any other sources, we have chosen not to include the corresponding results in the table.

The numerical solutions, surface plots and heatmaps, employing FVM-WSR with RBF $r^4 \log r$ and meshsize $h = \frac{1}{128}$ are illustrated in Fig. 5 at various time levels.

FVM-WSR offers the advantage of a lower computational cost in comparison to FVM-WENO, as it employs only one stencil for each reference volume. Table 3 presents a comparison of running times for both methods. Our experiments demonstrate (approximately) a 2x speedup with the new approach. There could still be some opportunities to speed up the WSR scheme when it comes to solving local linear systems of the form (5.2) for a varying diagonal matrix Λ. We will pursue these possibilities in our future studies.

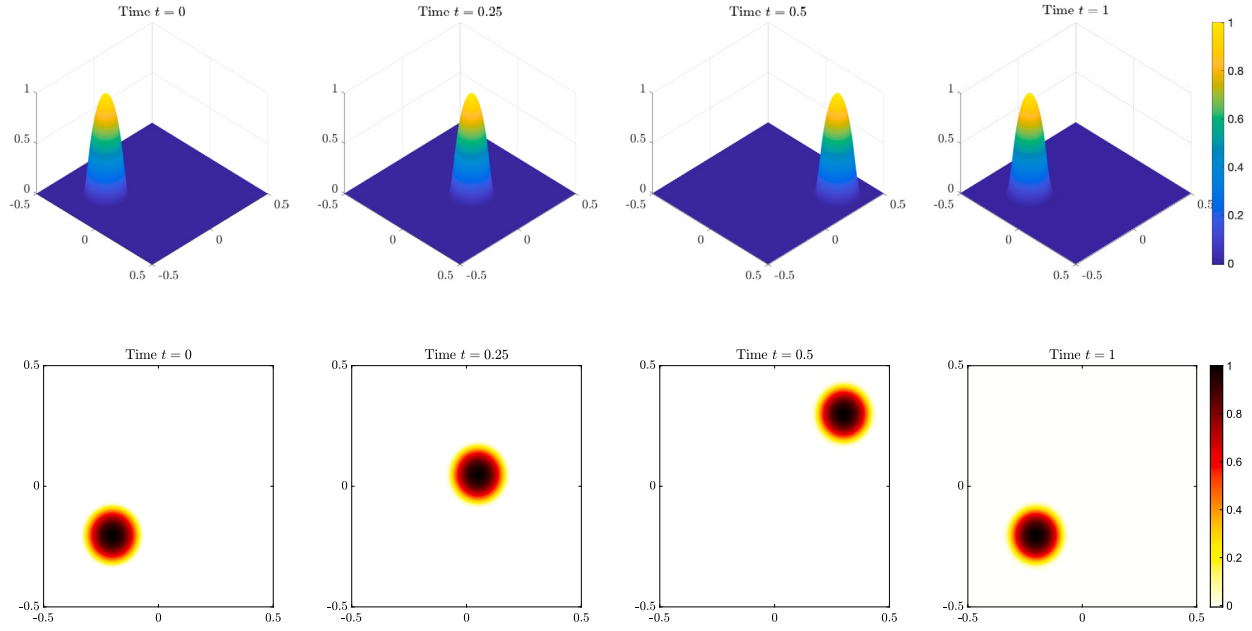

Fig. 6. The initial condition (6.3) (left plots) and numerical solutions using FVM-WSR for the advection equation at time levels $t = 0.25$, $t = 0.5$ and $t = 1$.

6.2. Linear advection with steep gradient or discontinuous initial conditions

Consider equation (6.1) defined on the same domain as before but with different initial conditions

$$u(0,x) = \begin{cases} \exp\left(\frac{\|x-c\|^2}{\|x-c\|^2-R^2}\right), & \|x-c\| < R, \\ 0, & \text{otherwise}, \end{cases} \tag{6.3}$$

and

$$u(0,x) = \begin{cases} 1, & \|x-c\| < R, \\ 0, & \text{otherwise}, \end{cases} \tag{6.4}$$

where $c = (-0.25, -0.25)$ and $R = 0.1$. These functions are depicted in the top-left of Figs. 6 and 7, respectively. As t increases, the initial profiles move in the direction $[1,1]$, but preserve their initial forms. Numerical solutions using FVM-WSR with RBF $\phi_{2,3}(r) = r^4 \log(r)$ and meshsize $h = \frac{1}{128}$ are presented in Figs. 6 and 7 at various time levels. In the reconstruction step, central stencils of $S_M(V)$ type are employed. Both cases exhibit minimal damping and oscillations, with slight smearing observed in the discontinuous solution. For a closer examination, we plot a cross-section of the solution along the direction $[1,1]$ (on the plane $x_1 = x_2$) at the final time in Fig. 8, and compare them with the exact and WENO solutions. We observe that the new method excels in capturing discontinuities. The same meshsize and temporal steplength are used for both methods. We followed the approach given in [3] to select the (forward and backward) stencils in the RBF-WENO method. However, one may opt for an alternative stencil selection or use a different oscillation indicator to enhance the result obtained by the WENO reconstruction.

6.3. Burgers' equation with a smooth initial condition

Consider the nonlinear Burgers' equation

$$u_t + uu_{x_1} + uu_{x_2} = 0, \tag{6.5}$$

where $u := u(t,x) : [0,t_f] \times [-0.5,0.5]^2 \longrightarrow \mathbb{R}$, with periodic boundary conditions and with initial condition (6.3) for $c = (-0.25,-0.25)$ and $R = 0.1$. As the time advances, a rarefaction develops behind the wave, while a shock forms in front of it. Numerical solutions using FVM-WSR with $h = \frac{1}{128}$ at time levels $t = 0.25$, $t = 1$ and $t = 2.3$ are shown in Figs. 9. Cross-section solutions on plane $x_1 = x_2$ at different time levels are also shown in Fig. 10. As we observe from the figures, the shock is perfectly captured and moves in the northeast direction without any significant oscillations. The polyharmonic RBF $\phi_{2,3}(r) = r^4 \log(r)$ and central stencils of type $S_M(V)$ are used in the reconstruction step.

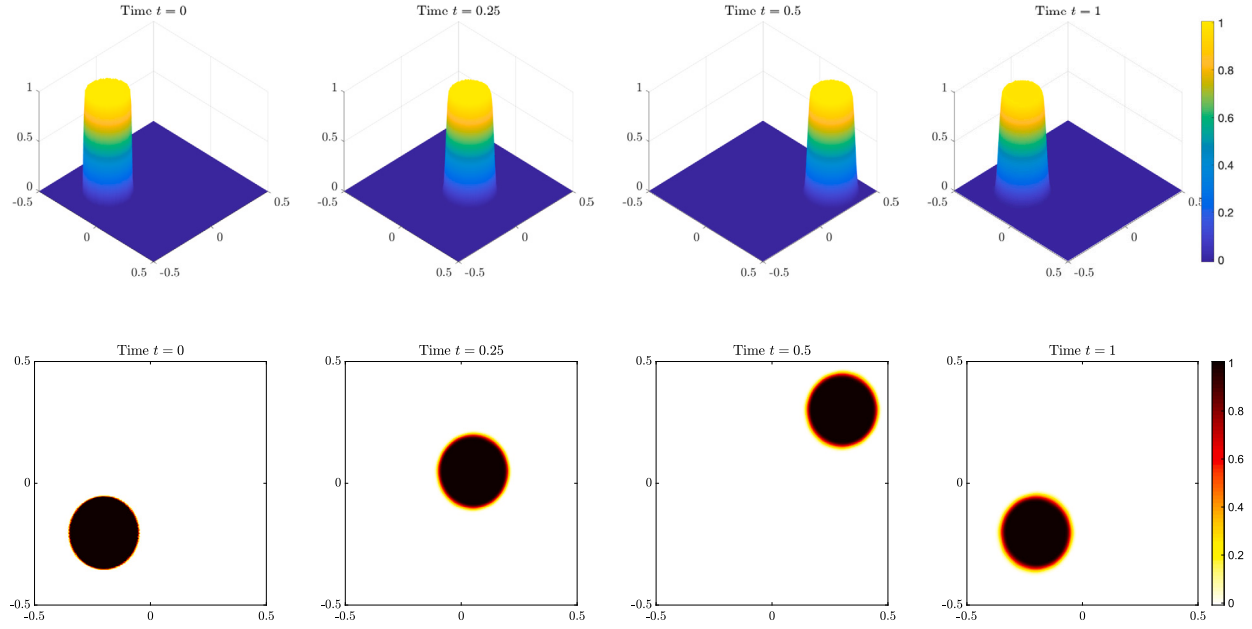

Fig. 7. The initial condition (6.4) (left plots) and numerical solutions using FVM-WSR for the advection equation at time levels $t = 0.25$, $t = 0.5$ and $t = 1$.

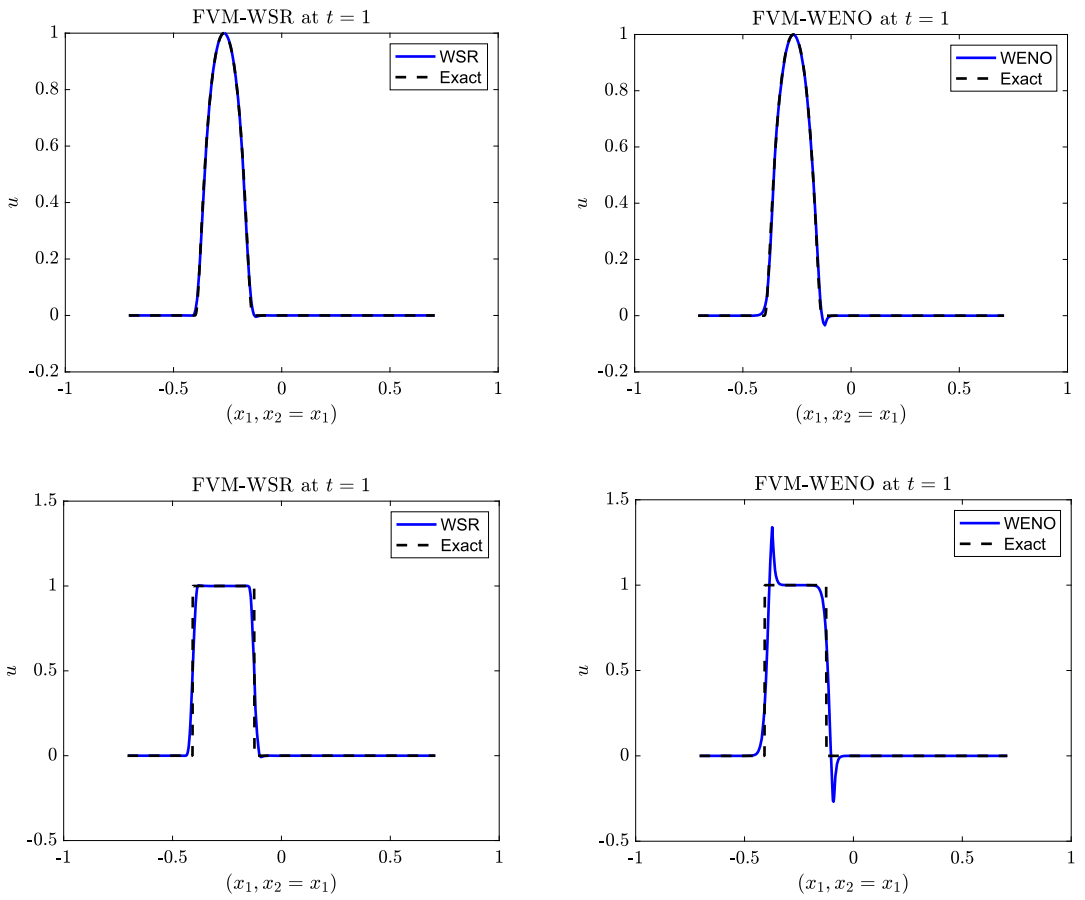

Fig. 8. The cross-section solutions in plane $x_1 = x_2$. Numerical solutions using WSR and WENO schemes with $h = 1/128$ are compared with exact solutions at final time $t = 1$ with initial condition (6.3) (first row) and initial condition (6.3) (second row).

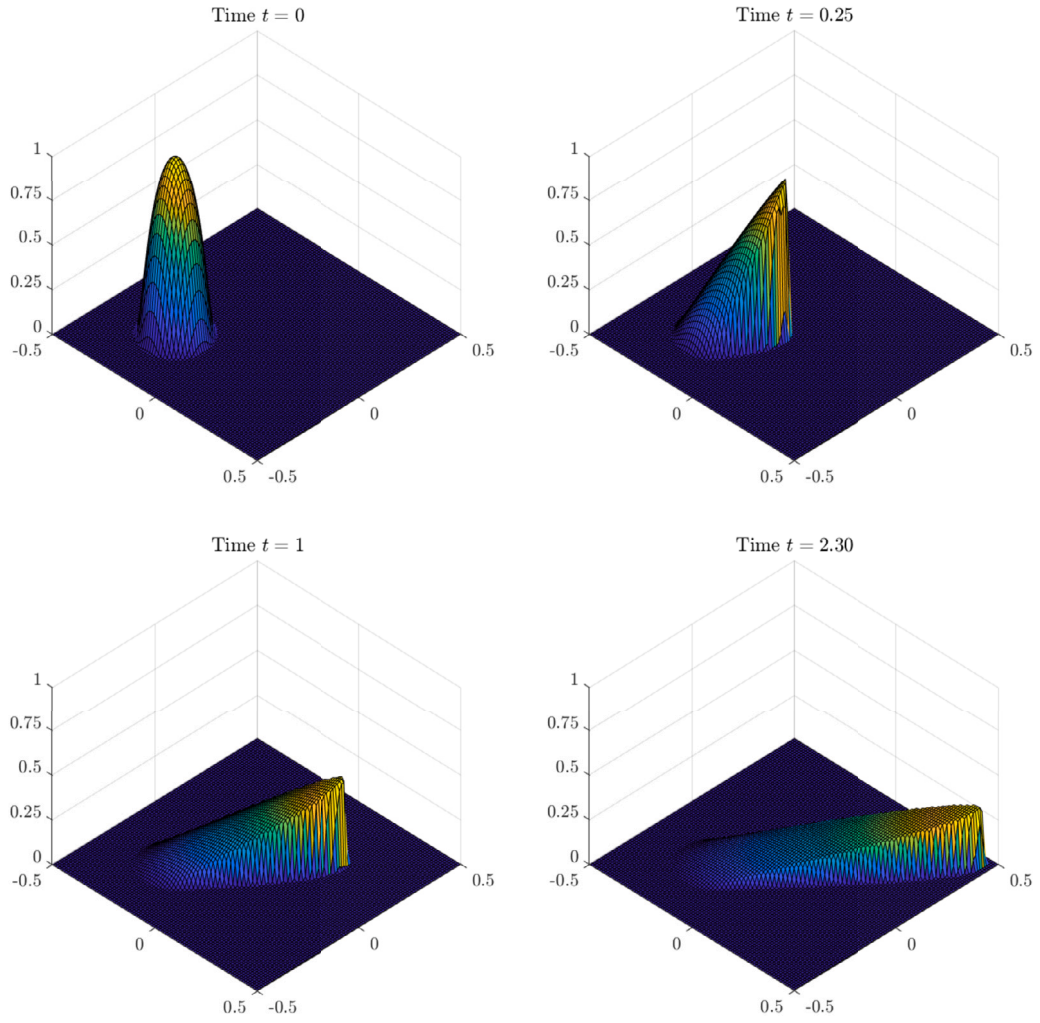

Fig. 9. The initial condition (upper left) and numerical solutions using FVM-WSR for the Burgers' equation at time levels $t = 0.25$, $t = 1$ and $t = 2.3$.

6.4. Burgers' equation with discontinuous initial condition

Consider the nonlinear Burgers' equation (6.5) for $u := u(t, x) : [0, 0.5] \times [0, 1]^2 \longrightarrow \mathbb{R}$, and with initial condition

$$u(0,x) = \begin{cases} -1.0, & \text{if } x_1 > 0.5,\ x_2 > 0.5, \\ -0.2, & \text{if } x_1 < 0.5,\ x_2 > 0.5, \\ 0.5, & \text{if } x_1 < 0.5,\ x_2 < 0.5, \\ 0.8, & \text{if } x_1 > 0.5,\ x_2 < 0.5. \end{cases} \tag{6.6}$$

The color contour plot of the (discontinuous) initial condition is shown in Fig. 11 (left panel). This is a challenging problem due to the emergence of different shocks and rarefaction waves as time increases. Following [19] we extend the problem domain to $[-1, 2]^2$ and apply a periodic boundary condition. The results are finally presented in the original domain $[0, 1]^2$. The plot of the FVM-WSR solution with meshsize $h = \frac{1}{128}$ at final time $t = 0.5$ is shown in Fig. 11. We have employed the polyharmonic RBF $\phi_{2,3}(r)$ and $S_M(V)$ stencils.

6.5. Kurganov-Petrova-Popov (KKP) rotating wave

Consider the rotating wave equation

$$u_t + \sin(u)u_{x_1} + \cos(u)u_{x_2} = 0, \tag{6.7}$$

where $u := u(t, x) : [0, 1] \times [-2, 2] \times [-2.5, 1.5] \longrightarrow \mathbb{R}$, with periodic boundary conditions and with initial condition

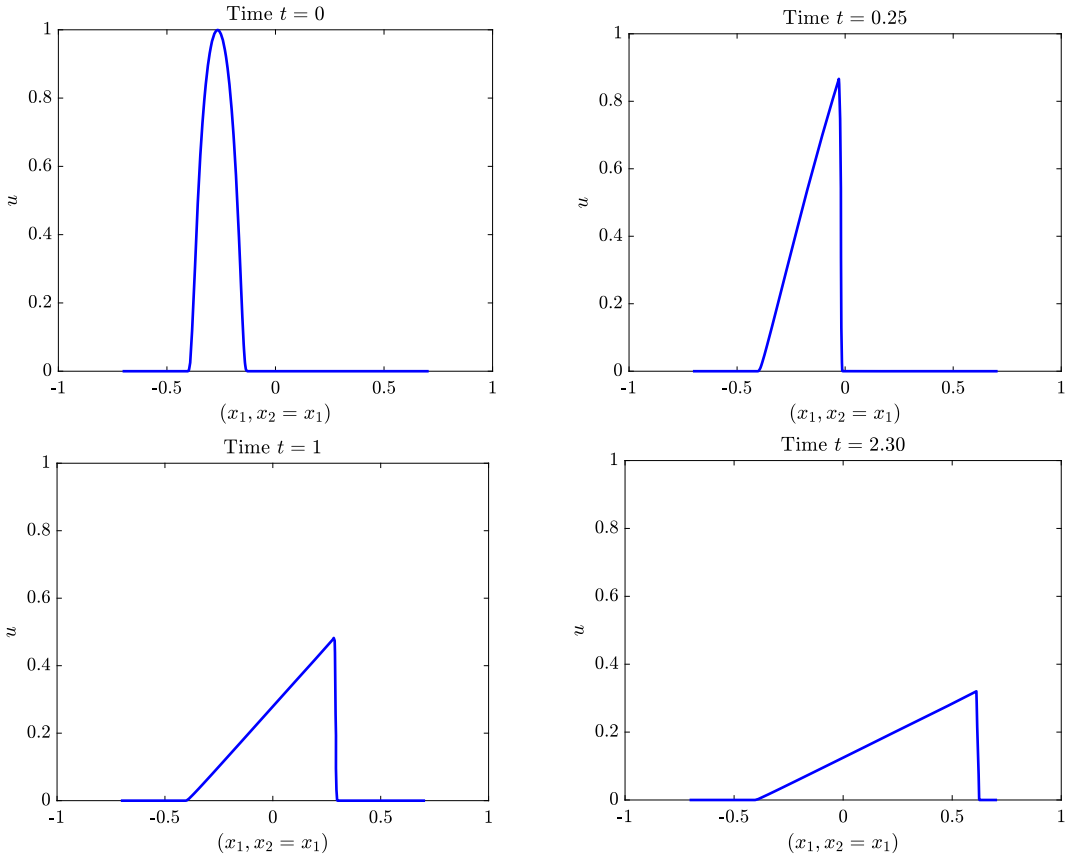

Fig. 10. Cross-section solutions at time levels $t = 0.25$, $t = 1$ and $t = 2.3$ for the Burgers' equation.

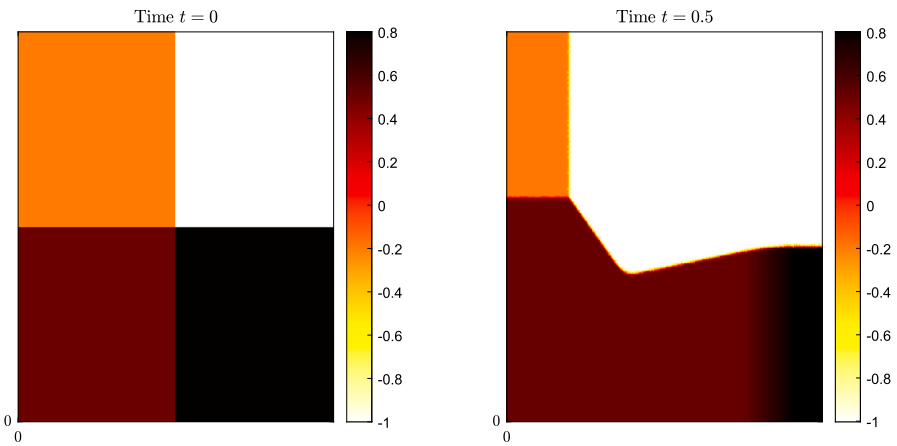

Fig. 11. The initial condition (6.6) (left) and FVM-WSR solution at final time $t = 0.5$.

$$u(0,x) = \begin{cases} 3.5\pi, & x^2 + y^2 < 1, \\ 0.25\pi, & \text{otherwise.} \end{cases} \tag{6.8}$$

The KKP problem, which involves nonconvex advective fluxes, was initially introduced by Kurganov [32] (see also [17,49]). This equation is specifically designed to serve as a test problem for evaluating different schemes in handling entropy-violating solutions. In Fig. 12, we present the FVM-WSR solution at the final time $t = 1$, computed with meshsize $h = \frac{1}{64}$. The reconstruction step employs the polyharmonic RBF $\phi_{2,3}$ and $S_M(V)$ stencils.

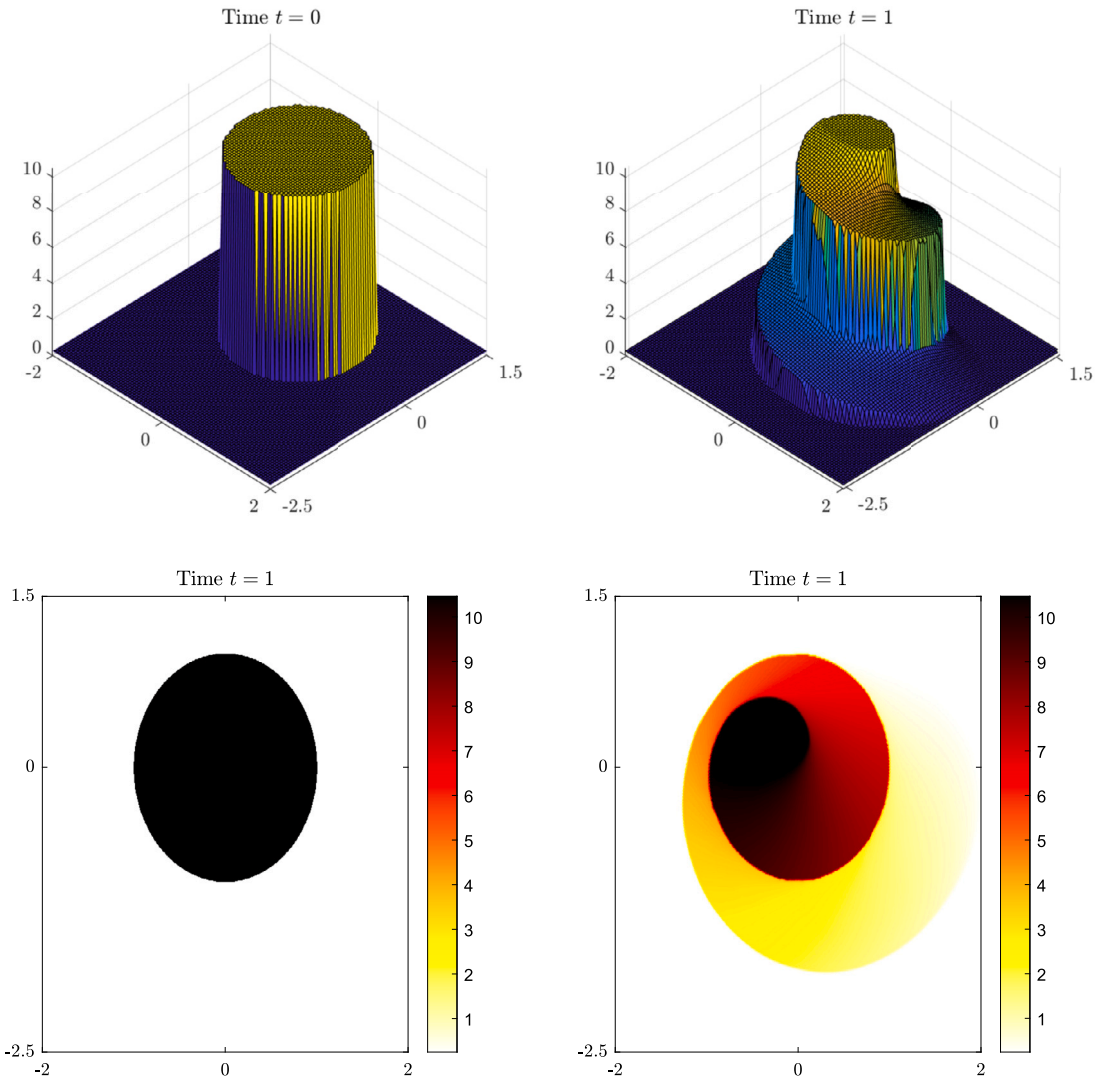

Fig. 12. The initial profile (left) and FVM-WSR solution at time $t = 1$ (right) for the KKP rotating equation.

7. Conclusions

In this paper, we introduced the novel FVM-WSR method for solving scalar conservation laws on unstructured meshes. This scheme incorporates a weighted smoothed reconstruction (WSR) and effectively suppresses nonphysical oscillations in the presence of discontinuities, shocks, and sharp fronts. Our experimental results show that this method achieves accuracy on par with (and sometimes superior to) other numerical approaches, such as RBF-WENO, while using only a single central stencil in its reconstruction step. This property contributes to the method's brevity, simplicity, and reduced computational cost. Additionally, this method can be easily adapted to deal with more complex problems such as 3D hyperbolic problems and systems of conservation laws. In an upcoming research paper, we will further extend the application of this technique for solving Euler's and Navier-Stokes equations.

CRediT authorship contribution statement

Davoud Mirzaei: Conceptualization, Formal analysis, Investigation, Methodology, Resources, Software, Supervision, Validation, Visualization, Writing – original draft, Writing – review & editing. **Navid Soodbakhsh:** Formal analysis, Investigation, Methodology, Resources, Software, Validation, Visualization, Writing – original draft, Writing – review & editing.

Declaration of competing interest

The authors declare the following financial interests/personal relationships which may be considered as potential competing interests: Navid Soodbakhsh reports financial support was provided by Institute for Research in Fundamental Sciences.

Data availability

Data will be made available on request.

References

[1] R. Abgrall, On ENO schemes on unstructured meshes: analysis and implementation, J. Comput. Phys. 114 (1994) 45–58.
[2] T. Aboiyar, E.H. Georgoulis, A. Iske, High order WENO finite volume schemes using polyharmonic spline reconstruction, in: Proceedings of the International Conference on Numerical Analysis and Approximation Theory, Cluj-Napoca (Romania), 2006, pp. 1–14.
[3] T. Aboiyar, E.H. Georgoulis, A. Iske, Adaptive ADER methods using kernel-based polyharmonic spline WENO reconstruction, SIAM J. Sci. Comput. 32 (2010) 3251–3277.
[4] T. Arbogast, C.S. Huang, M.H. Kuo, RBF WENO reconstructions with adaptive order and applications to conservation laws, J. Sci. Comput. 91 (2) (2022) 51.
[5] D.S. Balsara, S. Garain, V. Florinski, W. Boscheri, An efficient class of WENO schemes with adaptive order for unstructured meshes, J. Comput. Phys. 404 (2020) 109062.
[6] T.J. Barth, H. Deconinck, High Order Methods for Computational Physics, Springer Verlag, 1999.
[7] O. Davydov, R. Schaback, Optimal stencils in Sobolev spaces, IMA J. Numer. Anal. 39 (2019) 398–422.
[8] J. Duchon, Splines minimizing rotation-invariant semi-norms in Sobolev spaces, in: W. Schempp, K. Zeller (Eds.), Constructive Theory of Functions of Several Variables, Springer, Berlin, 1977, pp. 85–100.
[9] G.E. Fasshauer, Meshfree Approximations Methods with Matlab, World Scientific, Singapore, 2007.
[10] O. Friedrich, Weighted essentially non-oscillatory schemes for the interpolation of mean values on unstructured grids, J. Comput. Phys. 144 (1998) 194–212.
[11] S. Gottlieb, On high order strong stability preserving Runge-Kutta and multi step time discretization, J. Sci. Comput. 25 (2005) 105–127.
[12] S. Gottlieb, C.W. Shu, Total variation diminishing Runge-Kutta schemes, Math. Comput. 67 (1998) 73–85.
[13] S. Gottlieb, C.W. Shu, E. Tadmor, Strong stability preserving high order time discretization methods, SIAM Rev. 43 (2001) 89–112.
[14] J.L. Guermond, R. Pasquetti, B. Popov, Entropy viscosity method for nonlinear conservation laws, J. Comput. Phys. 230 (2011) 4248–4267.
[15] A. Harten, S.R. Chakravarthy, Multidimensional ENO schemes for general geometries, Technical Report, ICASE, 221:91–76, 1991.
[16] A. Harten, B. Engquist, S. Osher, S.R. Chakravarthy, Uniformly high order accurate essentially non-oscillatory schemes III, J. Comput. Phys. 71 (1987) 231–303.
[17] J.S. Hesthaven, Numerical Methods for Conservation Laws: From Analysis to Algorithms, SIAM, 2017.
[18] J.S. Hesthaven, F. Monkeberg, Entropy stable essentially nonoscillatory methods based on RBF reconstruction, ESAIM, M2AN 53 (3) (2019) 925–958.
[19] J.S. Hesthaven, F. Monkeberg, Two-dimensional RBF-ENO method on unstructured grids, J. Sci. Comput. 82 (3) (2020) 1–24.
[20] C. Hu, C.W. Shu, Weighted essentially non-oscillatory schemes on triangular meshes, J. Comput. Phys. 150 (1999) 97–127.
[21] T.J.R. Hughes, T.E. Tezduyar, Finite element methods for first-order hyperbolic systems with particular emphasis on the compressible Euler equations, Comput. Methods Appl. Mech. Eng. 45 (1984) 217–284.
[22] A. Iske, On the approximation order and numerical stability of local Lagrange interpolation by polyharmonic splines, in: International Series of Numerical Mathematics, vol. 145, Birkhäuser Verlag, Basel, 2003, pp. 153–165.
[23] A. Iske, On the construction of kernel-based adaptive particle methods in numerical flow simulation, in: Notes on Numerical Fluid Mechanics and Multidisciplinary Design (NNFM), Springer, Berlin, 2013, pp. 197–221.
[24] L. Ivan, C.P.T. Groth, High-order solution-adaptive central essentially non-oscillatory (CENO) method, J. Comput. Phys. 275 (2014) 830–862.
[25] Z. Ji, T. Liang, L. Fu, A class of new high-order finite-volume TENO schemes for hyperbolic conservation laws with unstructured meshes, J. Sci. Comput. 92 (2) (2022) 61.
[26] Z. Ji, T. Liang, L. Fu, High-order finite-volume TENO schemes with dual ENO-like stencil selection for unstructured meshes, J. Sci. Comput. 95 (3) (2023) 76.
[27] G. Jiang, C.W. Shu, Efficient implementation of weighted ENO schemes, J. Comput. Phys. 126 (1996) 202–228.
[28] C. Johnson, A. Szepessy, Shock-capturing streamline diffusion finite element methods for nonlinear conservation laws, in: T.J.R. Hughes, T.E. Tezduyar (Eds.), Recent Developments in Computatioonal Fluid Dynamics, AMD, New York, 1988, pp. 75–92.
[29] L. Kadrnka, The Finite Volume Particle Method: a Meshfree Method of Second Order for the Numerical Solution of Hyperbolic Conservation Laws, PhD thesis, Universität Hamburg, Hamburg, 2014.
[30] M. Kaser, A. Iske, ADER schemes on adaptive triangular meshes for scalar conservation laws, J. Comput. Phys. 205 (2005) 486–508.
[31] D. Kroner, Numerical Schemes for Conservation Laws, John Wiley and Sons, 1997.
[32] A. Kurganov, G. Petrova, B. Popov, Adaptive semidiscrete central-upwind schemes for nonconvex hyperbolic conservation laws, SIAM J. Sci. Comput. 29 (2007) 2381–2401.
[33] P.D. Lax, Weak solutions of nonlinear hyperbolic equations and their numerical approximation, Commun. Pure Appl. Math. 7 (1954) 159–193.
[34] R.J. LeVeque, Finite Volume Methods for Hyperbolic Problems, Cambridge University Press, Cambridge, 2002.
[35] X.D. Liu, S. Osher, T. Chan, Weighted essentially non-oscillatory schemes, J. Comput. Phys. 115 (1994) 200–212.
[36] A. Meister, J. Struckmeier, Hyperbolic Partial Differential Equations: Theory, Numerics and Applications, Springer, 2002.
[37] D. Mirzaei, The direct radial basis function partition of unity (D-RBF-PU) method for solving PDEs, SIAM J. Sci. Comput. 43 (2021) A54–A83.
[38] K.W. Morton, T. Sonar, Finite volume methods for hyperbolic conservation laws, Acta Numer. 16 (2007) 155–238.
[39] M. Nazarov, J. Hoffman, Residual based artificial viscosity for simulation of turbulent compressible flow using adaptive finite element methods, Int. J. Numer. Methods Fluids 71 (2013) 339–357.
[40] L.L. Schumaker, Numerical Methods for Conservation Laws: From Analysis to Algorithms, Wiley-Interscience Publication, 1981.
[41] V. Shankar, G.B. Wright, A. Narayan, A robust hyperviscosity formulation for stable RBF-FD discretizations of advection-diffusion-reaction equations on manifolds, SIAM J. Sci. Comput. 42 (2020) A2371–A2401.
[42] J. Shi, Y.T. Zhang, C.W. Shu, Resolution of high order WENO schemes for complicated flow structures, J. Comput. Phys. 186 (2003) 690–696.
[43] C.W. Shu, High order ENO and WENO schemes for computational fluid dynamics, in: High Order Methods for Computational Physics, Springer, Berlin, 1991, pp. 439–852.
[44] C.W. Shu, High order weighted essentially nonoscillatory schemes for convection dominated problems, SIAM Rev. 51 (2009) 82–126.
[45] C.W. Shu, Essentially non-oscillatory and weighted essentially non-oscillatory schemes, Acta Numer. 29 (2020) 701–762.
[46] C.W. Shu, S. Osher, Efficient implementation of essentially non-oscillatory shock capturing schemes, J. Comput. Phys. 77 (1988) 439–471.
[47] C.W. Shu, S. Osher, Efficient implementation of essentially non-oscillatory shock capturing schemes, II, J. Comput. Phys. 83 (1989) 32–78.
[48] T. Sonar, On the construction of essentially non-oscillatory finite volume approximations to hyperbolic conservation laws on general triangulations: polynomial recovery, accuracy and stencil selection, Comput. Methods Appl. Mech. Eng. 140 (1997) 157–181.
[49] V. Stiernström, L. Lundgren, M. Nazarov, K. Mattsson, A residual-based artificial viscosity finite difference method for scalar conservation laws, J. Comput. Phys. 430 (2021) 110100.
[50] I. Tominec, M. Nazarov, Residual viscosity stabilized RBF-FD methods for solving nonlinear conservation laws, J. Sci. Comput. 94 (14) (2023).
[51] E.F. Toro, Riemann Solvers and Numerical Methods for Fluid Dynamics: A Practical Introduction, Springer, 2013.

[52] J. Von Neumann, R.D. Richtmyer, A method for the numerical calculation of hydrodynamic shocks, J. Appl. Phys. 21 (1950) 232–237.
[53] H. Wendland, Scattered Data Approximation, Cambridge University Press, 2005.
[54] H. Wendland, C. Rieger, Approximate interpolation with applications to selecting smoothing parameters, Numer. Math. 101 (2005) 729–748.
[55] W.R. Wolf, J.L.F. Azevedo, High-order ENO and WENO schemes for unstructured grids, Int. J. Numer. Methods Fluids 55 (2007) 917–943.
[56] N. Zhan, R. Chen, Y. You, Three-dimensional high-order finite-volume method based on compact WENO reconstruction with hybrid unstructured grids, J. Comput. Phys. 49 (2023) 112300.
[57] Y.T. Zhang, J. Shi, C.W. Shu, Y. Zhou, Numerical viscosity and resolution of high-order weighted essentially nonoscillatory schemes for compressible flows with high Reynolds numbers, Phys. Rev. E 68 (2003) 046709.